Research Article ISSN 2639-9466

Nanotechnology & Applications

Ecofriendly-Multifunctional Composite of Poly(Butylene Adipate-Co-Terephthalate)/Zirconium Phosphate/Cinnamon Oil

Freitas DFS[1], Araújo AMCF[2], Souza YCA[1], Albitres GAV[1], Garcia EE[1], Cestari SP[3], Miguel MAL[2] and Mendes LC[1]*

[1]*Universidade Federal do Rio de Janeiro, Instituto de Macromoléculas Professora Eloisa Mano, Centro de Tecnologia, Bloco J, Ilha do Fundão, Rio de Janeiro, RJ, Brazil.*

[2]*Universidade Federal do Rio de Janeiro, Instituto de Microbiologia Paulo de Góes, Centro de Ciências da Saúde, Bloco I, Ilha do Fundão, Rio de Janeiro, Brazil.*

[3]*Centre for Innovation in Polymer Engineering (PIEP), Universidade do Minho, Campus de Azurém, Edifício 15, 4800-058 Guimarães – Portugal.*

***Correspondence:**
Mendes LC, Universidade Federal do Rio de Janeiro, Instituto de Macromoléculas Professora Eloisa Mano, Centro de Tecnologia, Bloco J, Ilha do Fundão, Rio de Janeiro, RJ, Brazil.

Received: 14 Jan 2025; **Accepted:** 19 Feb 2025; **Published:** 12 March 2025

Citation: Freitas DFS, Araújo AMCF, Souza YCA, et al. Ecofriendly-Multifunctional Composite of Poly(Butylene Adipate-Co-Terephthalate)/Zirconium Phosphate/Cinnamon Oil. Nano Tech Appl. 2025; 8(1): 1-12.

ABSTRACT

The UN Agenda 2030 prescribes important actions aimed at environmental sustainability. Regarding plastics, the use of sustainable polymers is strongly encouraged. Over the centuries, cinnamon essential oil (CEO) has been used for various purposes, such as pharmaceutical, medicinal, agricultural, and bactericidal applications. This work was designed to combine the characteristics of cinnamon essential oil and zirconium phosphate (ZrP) in a poly(butylene adipate-co-terephthalate) (PBAT) matrix, to obtain an environmentally friendly and multifunctional composite. ZrP was synthesized and chemically modified. PBAT composite casting films with 2 wt.% of phosphate (pristine and modified) and CEO (0, 5, and 10 wt.%) were prepared. The intercalation of CEO caused the delamination of the phosphate lamellae. The interaction between CEO and PBAT depended on the amount of cinnamon oil. Hydrophobicity increased in the range of 27–51%, depending on the phosphate type and CEO content. PBAT's glass transition temperature (Tg) changed with the addition of CEO, as did the linear coefficient of thermal expansion (LCTE). Phosphates induced an increase in PBAT's degree of crystallinity. The effect of CEO on PBAT's molecular mobility depended on the type of phosphate applied. The incorporation of phosphate increased PBAT's degree of crystallization by almost two times. PBAT/ZrP/ED/CEO10 demonstrated an inhibition zone of around 12–14 mm against various Gram-positive and Gram-negative bacteria (GPB and GNB) and 32 mm against Candida albicans. The material has potential applications in the packaging sector (e.g., for fruits and vegetables) to extend shelf life, as well as in personal care products. Additionally, it helps prevent microplastic proliferation due to PBAT's biodegradable characteristics.

Keywords
Bactericidal, Hydrophobicity, Essential cinnamon oil, PBAT, Zirconium phosphate.

Introduction
The UN 2030 Agenda outlines several sustainable development goals, including reversing environmental degradation, halting biodiversity loss, promoting responsible consumption and production, combating climate change, fostering sustainable industrialization, and encouraging innovation. In this context, the search for sustainable materials is strongly encouraged [1].

Poly(butylene adipate-*co*-terephthalate) (PBAT) is a polymer primarily composed of aliphatic segments - butylene adipate -, which imparts biodegradability but results in poor mechanical properties. To address this limitation, inorganic fillers are used to create polymeric composites that enhance PBAT's properties and expand its applications [2]. Guo et al. investigated the

incorporation of sodium alginate-doped lignin nanoparticles (SLNPs) into a PBAT matrix, achieving improved mechanical properties and enhanced ultraviolet resistance [3]. Similarly, Wondun et al. studied composites containing barium titanate ($BaTiO_3$), multiwalled carbon nanotubes (MWCNTs), and PBAT, reporting significant improvements in mechanical strength, dielectric properties, thermal conductivity, and fire resistance [4].

To enhance compatibility with PBAT, Zhou et al. developed composites with fillers such as silanized montmorillonite and fractionated lignin. They found that even with a 60 wt.% filler content, mechanical properties remained stable, while water vapor and oxygen permeability were reduced by 40% and 90%, respectively [5]. Other studies have explored biofillers, such as mangosteen and durian peel waste, in PBAT composites. Although these fillers resulted in darker materials, they exhibited strong mechanical properties and thermal stability, making them promising for food and medical packaging applications [6]. Additionally, zinc oxide-supported diatomite was incorporated into a poly(lactic acid) (PLA)/PBAT blend. While some mechanical properties declined, antibacterial activity and thermal stability improved [7].

Cinnamon, derived from a tropical tree, has been valued for centuries for its diverse applications, including pest control, fruit and vegetable preservation, and antimicrobial, antioxidant, and anti-inflammatory properties [8-10]. Han and Parker studied cinnamon bark essential oil (CBEO) and found that it exhibited strong anti-proliferative effects on skin cells while inhibiting inflammatory biomarkers and tissue remodeling molecules [11]. Cinnamon essential oil (CIEO) has also been integrated into polymer matrices, such as carboxymethyl cellulose/quaternized starch (CMC/MS-Q188), to create biocomposites for wound dressings. These materials demonstrated strong antimicrobial properties against both Gram-positive and Gram-negative bacteria [12]. Hussein et al. developed nanofibrous membranes using polyurethane/poly(vinyl alcohol)-gelatin (PU/PVA-Gelatin) infused with cinnamon essential oil (CEO) and nano-cerium oxide ($nCeO_2$). Their results showed enhanced mechanical and thermal properties, along with inhibited growth of *Staphylococcus aureus* and *Escherichia coli* [13].

Layered transition metal phosphates have been studied since the late 1950s. As part of the 2D material family, they have a high ion exchange capacity, allowing chemical modifications with hydrophilic and hydrophobic compounds. This versatility has broadened their applications in nanotechnology [14-16]. Over the past four years, numerous studies have explored the use of zirconium phosphate (ZrP) in polymeric nanocomposites, particularly for flame retardant applications [17-27]. Kojima et al. investigated ZrP as a protein adsorbent and enzyme immobilization substrate, attributing its enhanced catalytic activity to its mesoporous structure and modified three-dimensional framework [28]. ZrP has also been chemically modified with polyetheramine, 1,3-epoxy-3-phenoxypropane, and cyclohexene oxide in sequence. These modifications led to ZrP exfoliation, improved dispersion in epoxy resin, increased composite modulus, and reduced thermal expansion [29]. Additionally, ZrP nanoparticles have been incorporated into epoxy resin to develop intraradicular dental posts. Laser scanning confocal microscopy and atomic force microscopy revealed good adhesion between the filler and polymer matrix, as well as variations in filler dispersion and distribution [30].

The development of sustainable and multifunctional materials remains a significant challenge. Therefore, this study aims to combine the biodegradability of PBAT, the structural properties of ZrP, and the multifunctionality of cinnamon. The resulting material has potential applications in packaging and personal care products, offering an innovative approach to environmentally friendly composite development.

Experimental

Materials

Table 1 describes the materials used in the experiment.

Material	Caracteristic	Origin
Poly(butylene adipate-terephthalate)	PBAT (Ecoflex® F Blend C 1200)	BASF S.E.
Phosphoric acid	H_3PO_4	Sigma-Aldrich Co.
Zirconium (IV) oxide chloride 8-hydrate	$Zr(O)Cl_2.8H_2O$	Sigma-Aldrich Co.
Ethyl alcohol	$C(H_3)$-$C(H_2)OH$	Sigma-Aldrich Co.
Ethylenediamine	$H_2NC(H_2)C(H_2)NH_2$	Tedia Brazil
Essential Cinnamon oil	(Cinnamaldehyde) 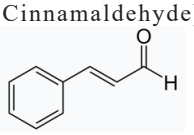	Phytotratha Cosmeticos Ltda

Synthesis and Modification of Zirconium Phosphate

Synthesis and intercalation of zirconium phosphate [31] are summarized in Table 2.

Table 2: Brief of ZrP synthesis and intercalation.

ZrP Synthesis	Ratio	Temperature °C	Time h	Label
12M H_3PO_4	Zr:P = 18	110	24	ZrP
$ZrOCl_2 \cdot 8H_2O$				
ZrP Intercalation				
ZrP	1:1	25	24	ZrP/ED
$H_2NC(H_2)C(H_2)NH_2$				

Composite and specimen preparation

Casting films of PBAT/ZrP and PBAT/ZrP/ED were obtained by mixing the PBAT chloroform solution with ZrP or ZrP/ED chloroform dispersion (2 wt.%). For films containing ECO, the ECO was added to the phosphate dispersion (5 and 10 wt.% based on PBAT content) following its mixing with PBAT solution. The final dispersion was poured onto a Petri dish and placed in an oven for drying. A PBAT film without additives was prepared for comparison Films were classified as PBAT, PBAT/ZrP, PBAT/ZrP/ED, PBAT/ZrP/ECO_5, PBAT/ZrP/ED/ECO_5, and PBAT/ZrP/ED/ECO_{10}. Figure 1 presents a schematic representation of the experimental procedure.

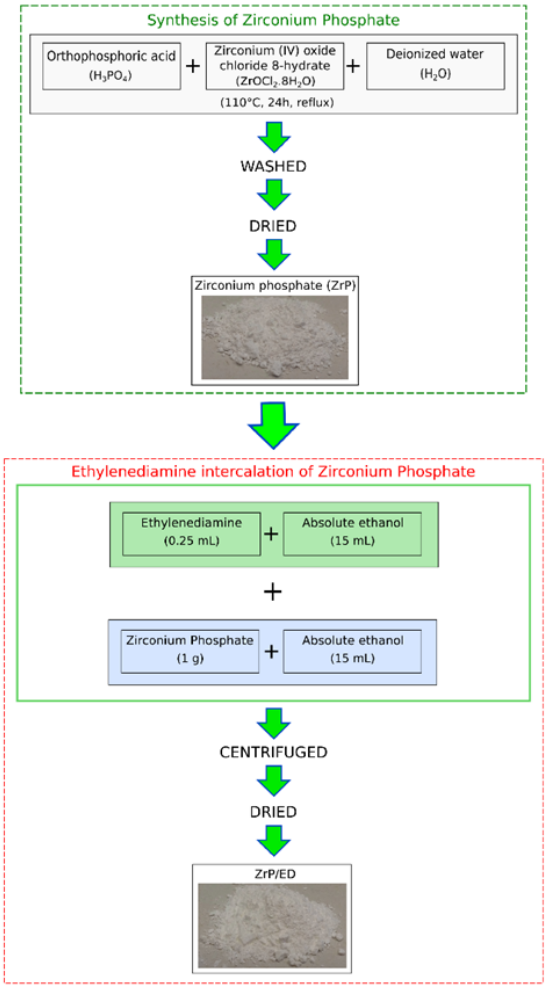

Figure 1a: Synthesis of Zirconium phosphate and ethylenediamine intercalation.

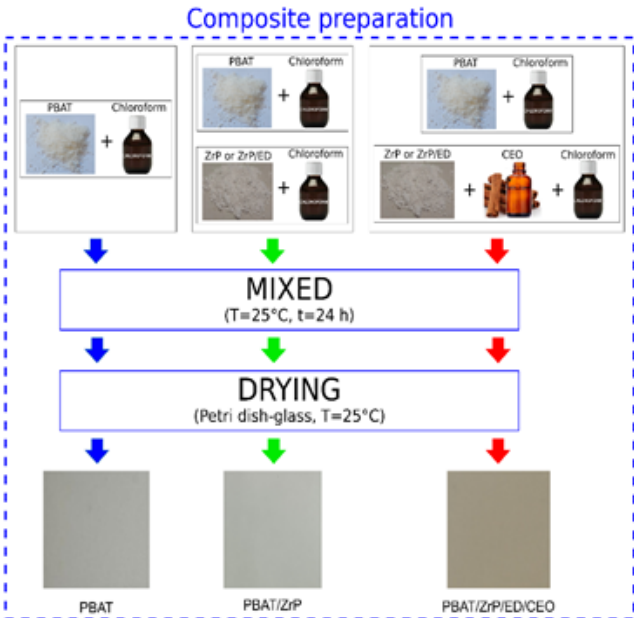

Figure 1b: Composite preparation.

Characterization

Fourier transform infrared spectroscopy (FTIR) was conducted in a Perkin Elmer Frontier model equipment, by ATR mode, in the spectral range 4000–600 cm^{-1}, 60 scans, resolution of 4 cm^{-1}. **Wide-angle X-ray diffraction (WAXD)** was performed in a Rigaku equipment model Ultima IV, CuKα radiation (1.5418 Å), a Ni filter, 30 kV voltage, current of 15 mA, diffraction angle (2θ) ranging from 2° to 50°, with a resolution of 0.05º. **Thermogravimetry (TG/DTG)** was carried out in a TA Instruments Q500, from 10 to 700°C, at 10°C/min, with nitrogen as the carrier gas. T_{onset}, T_{max}, and T_{50} (50 wt.% mass loss) were recorded. **Differential scanning calorimetry (DSC)** was conducted in a TA Instruments Q1000 model. Three heating routes were performed (first, third, and fifth cycles, 15-190°C, 10°C/min) and two cooling ones (second cycle (quenching) and fourth cycle). Crystallization and melting temperatures (T_c and T_m) were taken. The degree of crystallinity (X_c) was determined based on the ratio of the experimental melting enthalpy to the melting enthalpy of 100% crystalline PBAT (114 J/g) [32]. **Thermomechanical analysis (TMA)** was performed in a TMA 450 Discovery (TA Instruments), using a macroextension probe with 0.2 N, -50 to 0°C, 10°C/min, under a nitrogen atmosphere. Glass transition temperature (T_g) and the linear coefficient of thermal expansion (LCTE) were monitored according to ISO 11359-2:2021 [33]. **Wettability evaluation. Contact angle** (θ) was recorded using an OCA15EC – Dataphysics Instruments, with the aid of the coupled filming apparatus and software, dpiMA, in triplicate. **Time domain hydrogen nuclear magnetic resonance (TD NMR)** was conducted using a MARAN Ultra 0.54 T system (23.4 MHz for 1H) from Oxford Instruments, equipped with an 18 mm probe. All data were collected at 30°C, and the 90° pulse length was automatically calibrated to 7.5 µs. The longitudinal relaxation time (T_1H) was determined from the relaxation curve. **Microbiological evaluation:** Gram-positive bacteria (GPB) and Gram-negative bacteria (GNB) were obtained from the culture collection of the Institute of Microbiology Paulo de Góes at UFRJ. The GNB bacteria studied included *Escherichia coli* (American Type Culture Collection [ATCC] 11229), *Salmonella Enteritidis* ATCC 13076, and *Pseudomonas aeruginosa* ATCC 15442. The GPB tested were *Staphylococcus aureus* ATCC 29213, *Listeria monocytogenes* ATCC 19117, and *Bacillus cereus* ATCC 14579. Additionally, the yeast *Candida albicans* ATCC 10231 was included in the evaluation. The microorganisms were activated for the experiments. Bacteria were cultivated in 5 mL of liquid culture medium (Brain Heart Infusion [BHI], Merck) for 24 h, while *Candida albicans* yeast was propagated in Sabouraud Broth (Merck) for 48 h. Both bacteria and yeast were incubated at 37 °C. Five colonies from each microorganism were used to prepare a suspension in 0.85% (w/v) saline solution, achieving a cell concentration of approximately 10^8 colony-forming units per milliliter (CFU/mL). The standardized inoculum for each microorganism was spread onto the surface of BHI agar plates (for bacteria) or Sabouraud agar plates (for yeast) using a sterile swab (wooden rod with a cotton tip) in three different directions to ensure confluent microbial growth. Disks of 6 mm were carefully placed on the agar surface under aseptic conditions. The inoculated plates were incubated at 37 °C, for 48 h. Antibacterial activity was

assessed by measuring the zone of inhibition (mm) against each test organism. All experiments were performed in triplicate.

Results and Discussion

Fourier Transform Infrared spectroscopy (FTIR)

Figure 2 shows the infrared spectra of the samples, along with the spectral regions of 4,000-3,000 and 1,200-800 cm^{-1}. Table 3 summarizes the main absorptions extracted from the samples' spectra. PBAT presents as main absorptions at 2,956 cm^{-1} (C-H vibration in methylene group), 1,710 cm^{-1} (C=O of ester group vibration), 1,268 and 1,103 cm^{-1} (O-C-O linkage vibration), 870 cm^{-1} (C-H bending vibration in phenyl ring) and 725 cm^{-1} (methylene group vibration). Highlighted CEO absorptions were considered at 1,679 and 1,626 cm^{-1} (C=O carbonyl aldehyde vibrations), 1,573 cm^{-1} (C=C vibration in phenyl ring), 1,449 cm^{-1} (C-O-H bending vibration), 1,293 cm-1 (CH_2 in plane bending vibration), 1,248 and 1,124 cm-1 (C-O-C and C-O stretching vibrations), 1,071 cm-1 (C-O-H deformation vibration), 970 cm^{-1} (C-H bending vibration), 745 cm-1 (=C-H vibration in phenyl ring) and 687 cm^{-1} (C=C linkage vibration). For PBAT/ZrP, besides copolymer vibrational modes absorptions at 3,590 cm^{-1} (free P-O-H groups vibration), 3,508 (hydrogen bonding between P-O-H groups and H-O-H molecules), 3,138 cm^{-1} (telescopic vibration mode of P-O-H groups), 1,270 and 1,250 cm^{-1} (HPO_4^{2-} groups vibration) and 1,026 cm^{-1} (P-O linkage vibrational deformation) were attributed to ZrP. In the spectra of PBAT/ZrP/CEO_5, PBAT/ZrP/ED, PBAT/ZrP/ED/CEO_5 and PBAT/ZrP/ED/CEO_{10} PBAT absorptions prevailed [34-38]. Detailed visualization of the spectral regions at 4,000-3,000 and 1,200-800 cm^{-1} indicated influences of phosphates and CEO on the spectra outline. Between 4,000-3,000 cm^{-1}, the spectra of PBAT, PBAT/ZrP/ED, and PBAT/ZrP/ED/CEO_{10} showed similar shape. Clearly, the composite PBAT/ZrP induced to infer that there was not any interaction between polymer and phosphate. After CEO addition, that composite revealed a decrease in the intensity of ZrP absorptions indicating that CEO penetrated the ZrP galleries reducing the interaction between its nanolamellae to some extent. The spectrum of the composite PBAT/ZrP/ED/CEO_5 showed new absorption around 3,400 cm^{-1} and 3,200-3,000 cm^{-1} which could be associated with the formation of hydrogen bonds between free P-O-H groups and the carbonyl group of CEO. Similar behavior was observed in the range 1,200-800 cm^{-1}. PBAT, PBAT/ZrP/ED, and PBAT/ZrP/ED/CEO_{10} showed overlapping spectra. PBAT/ZrP evidenced the phosphate absorptions while the CEO addition caused a reduction in the intensity of this absorption. The expansion of the PBAT/ZrP/ED/CEO_5 endorsed the formation of hydrogen bonding between free P-O-H groups and the carbonyl group of CEO. In summary, the polymer/phosphate and polymer/CEO interactions were specific to each composite studied.

Wide-angle X-ray diffraction (WAXD)

Figure 3 presents a compilation of samples' X-ray diffraction patterns. PBAT showed two diffraction angles around 16 and 17° corresponding to basal reflections (011) and (010) as reported by Fukushima and collaborators [39]. The diffraction pattern of PBAT/ZrP showed the main reflections of ZrP around 12, 20, and 25° associated with Miller indexes (002), (110) and (112), respectively [40]. Upon adding CEO to PBAT/ZrP, those reflections still remained but with lower intensity. For PBAT/ZrP/ED, the reflection around 12° was displaced to lower angles while those around 20 and 25° disappeared, indicating that ED disrupted the lamellar crystalline structure of ZrP to some extent. The incorporation of CEO into the PBAT/ZrP/ED caused the complete delamination of the crystalline arrangement of ZrP. The delamination influenced the PBAT crystallization, as seen in the PBAT/ZrP/ED/CEO10, where the PBAT diffraction angles around 16 and 17° appeared. Venkatesan et al. prepared films based on a composite of PBAT embedded with silver vanadium oxide (AgVO3). The authors noted the improvement of the PBAT crystalline phase by filler addition [41]. For better understanding, a sketch of the phosphate intercalation and delamination induced by ED and CEO is presented in Figure 4. The results are consistent with the FTIR analysis.

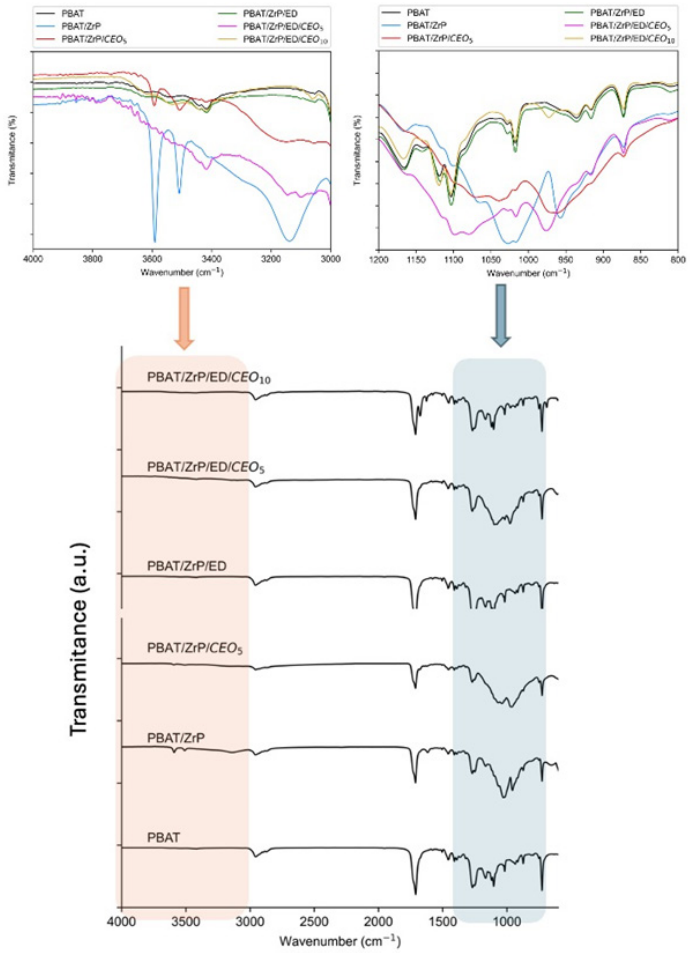

Figure 2: Total and partial visualization of FTIR spectra.

Thermogravimetry

Figure 5 presents the TGA loss mass and derivatives curves. The PBAT/ZrP and PBAT/ZrP/CEO_5 loss mass curves are nearly identical to the PBAT one, while the PBAT/ZrP/ED/

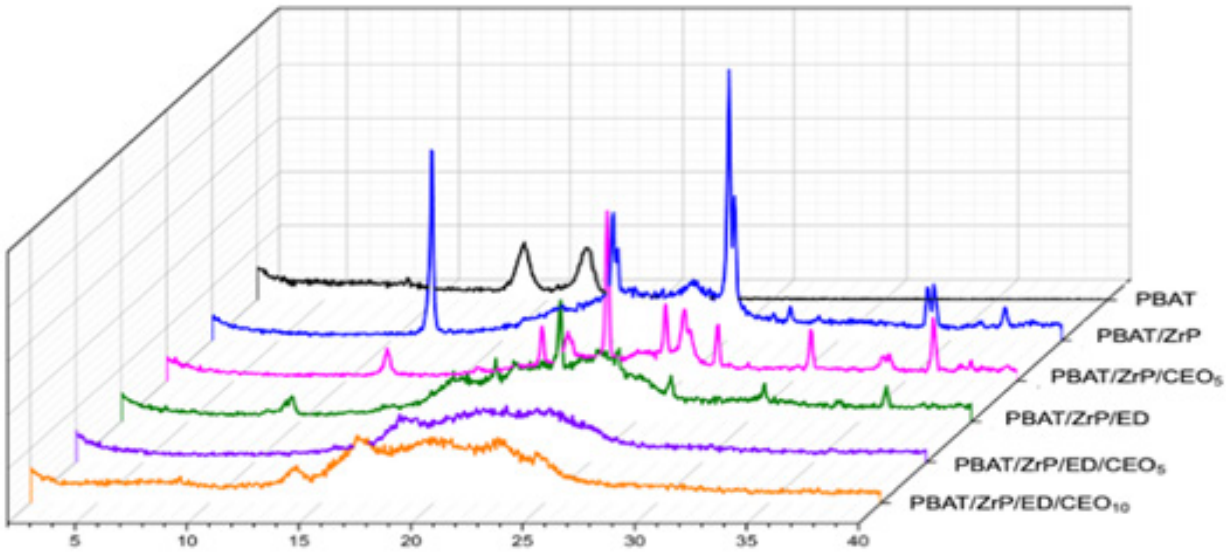

Figure 3: Compilation of samples' X-ray diffraction patterns.

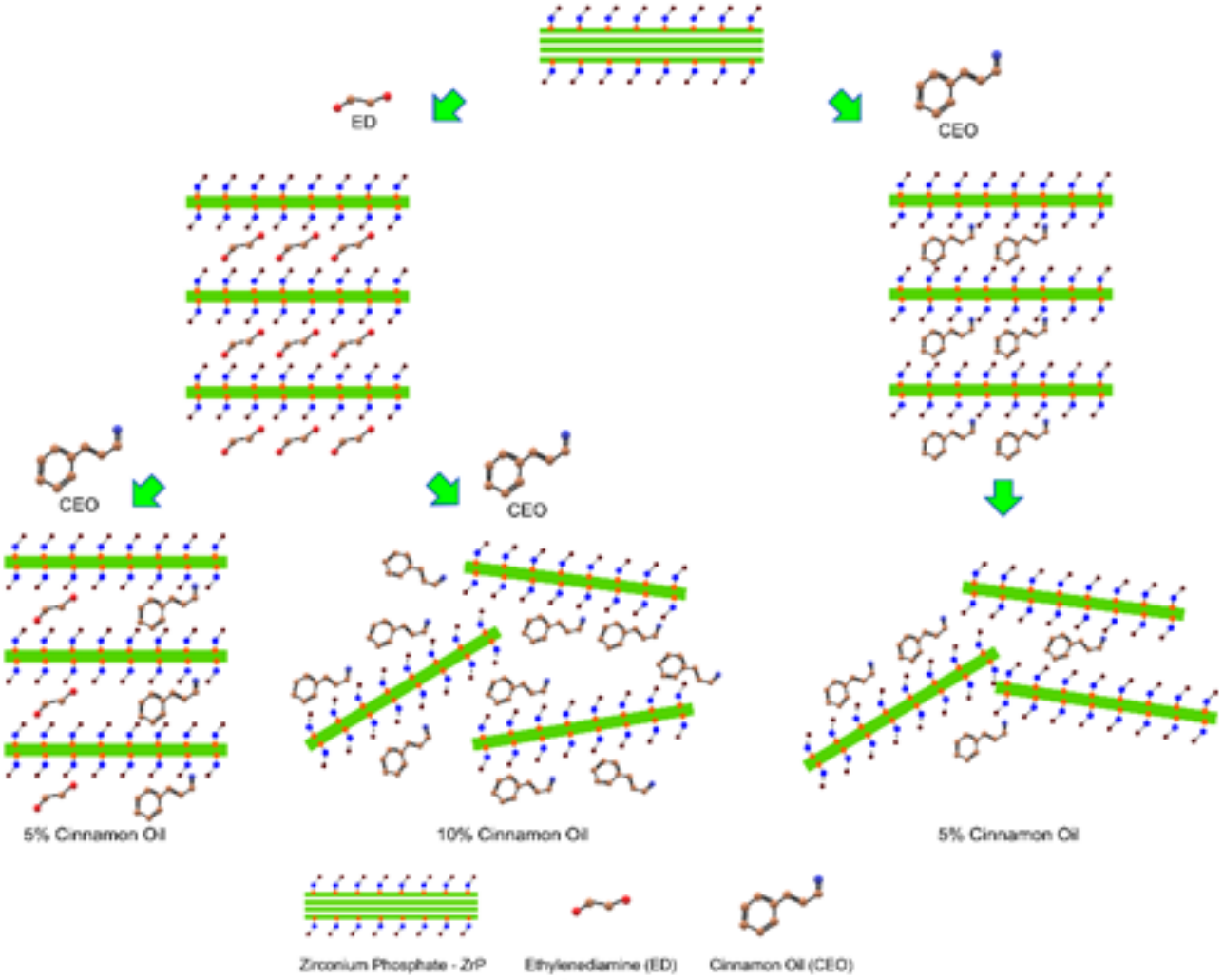

Figure 4: Schematic representation of ED- and CEO-induced intercalation and delamination in ZrP lamella.

Table 3: Compilation of the infrared absorptions of the samples.

Sample	Absorption (cm-1)	Reference
PBAT	**2956**,**1710**,1504,1457,1409,1390, **1268**,1252,1206,1165,1118, **1103**,1017, 935, 916, **873**, 750, **726**	Sim et al., 2019
CEO	3466, 3028, 2923, 2813,2740, **1671**, **1624**, 1605, **1575**, 1513,1495,**1449**,1378,**1293**,1269,**1250**, 1203, 1178, 1159, **1120**, **1071**, 1005, **970**, 918, 842, **745**, **687**, 605	Li et al., 2013
PBAT/ZrP	**3590**, **3508**, **3138**, 2957,1711,1616,1504,1458,1409,1389,**1270**, **1250**,1165,**1026**,1016, 957, 873, 750, 726, 654	Sim et al., 2019 and Li et al., 2024
PBAT/ZrP/CEO$_5$	2956,1711,1452,1409,1269,1039, 962, 872, 748, 726	Li et al., 2013, Sim et al., 2019 and Li et al., 2024
PBAT/ZrP/ED	2957,1710,1504, 1457, 1409, 1389, 1267,1251, **1206**,1166,1141,1117, 1102,1017, 935, 916, 873, 810, 750, 726	Sim et al., 2019, Li et al., 2024, Yan et al., 2023
PBAT/ZrP/ED/CEO$_5$	2957, 1711,1504,1458, 1409, 1389, 1269, 1098, 1079, 1016, 976, 916, 873, 749, 726	Li et al., 2013, Sim et al., 2019 and Li et al., 2024, Yan et al., 2023
PBAT/ZrP/ED/CEO$_{10}$	2956, 1711, 1675,1626, 1576, 1504, 1451, 1409, 1390, 1267, 1252, 1166, 1119, 1103,1017, 972, 935, 916, 873, 749, 727, 690, 605	Li et al., 2013, Sim et al., 2019 and Li et al., 2024, Yan et al., 2023

CEO$_5$ and PBAT/ZrP/ED/CEO$_{10}$ curves deviate either upwards or downwards from the PBAT one depending on the oil content. Most DTG curves revealed one step of degradation with no significant variation in T_{max}, except for PBAT/ZrP/ED/CEO$_{10}$ where an additional peak appears with T_{max} around 200 °C. Table 4 summarizes the thermogravimetric data. For the composites, T_{onset} increased slightly due to ZrP, while the addition of CEO induced a slight decrease. In general, T_{max} showed a minor increase, mainly due to the addition of ZrP. Analysis of T_{10}, $T_{25,}$ and T_{50} showed that almost 50 wt.% of the PBAT degraded near the $T_{max,}$. This degradation was associated with the aliphatic segment of the copolymer (butylene adipate). The additional degradation peak that emerged around 190 °C does not affect the production of blown films of the composite, as published by Singh et al., where the PBAT processing window is constricted to 125-140 °C [42]. Han et al. prepared a new nanoparticle through self-assembly of ZnO, tannic acid (TA) and cetyltrimethylammonium bromide (CTAB). Despite incorporating around 17 wt.% of ZnO, no change in thermal stability was observed [43]. In summary, the presence of phosphate and CEO does not significantly impact the thermal stability of the composites at low temperatures, and thus, does not hinder their use as sustainable films for the packaging sector.

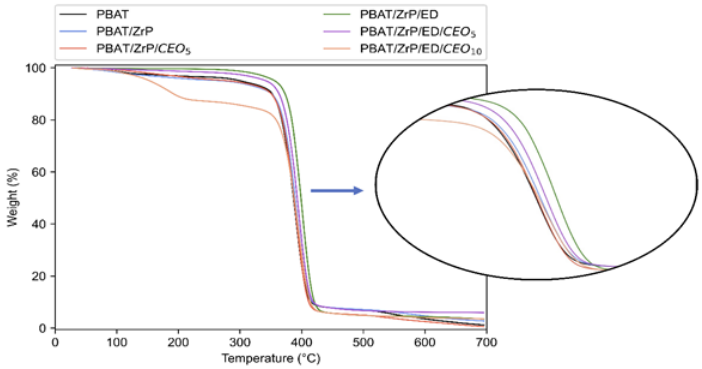

Figure 5a: Loss mass curves.

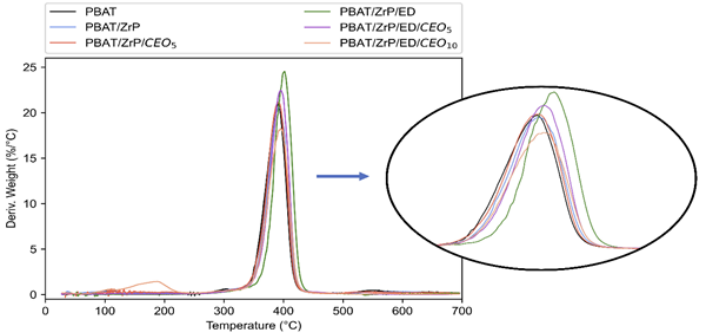

Figure 5b: DTG curves

Table 4: TGA data.

Sample	T_{onset} (ºC)	T_{max} (ºC)	Residue (%)	T_{10} (ºC)	T_{25} (ºC)	T_{50} (ºC)
PBAT	364	391	1.2	353	372	387
PBAT/ZrP	368	392	2.7	351	374	389
PBAT/ZrP/ED	378	402	3.5	373	387	399
PBAT/ZrP/CEO$_5$	367	391	0.5	351	373	387
PBAT/ZrP/ED/CEO$_5$	372	396	3.0	363	380	393
PBAT/ZrP/ED/CEO$_{10}$	188/370	395	3.5	193	368	388

Differential Scanning Calorimetry

Figure 6 shows the thermal curves of the 1st and 3rd heating cycles and 2nd cooling cycle. Except for PBAT, the 1st heating curves revealed that all composites exhibited two melting peaks around 40-60 and 100-145 °C. The crystallization temperature (T_c) presented quasi-flattened and low-intensity peaks, indicating that crystallization occurred over a wide temperature range. The presence of phosphates shifted the crystallization peak to higher temperatures, while ECO caused a shift to lower temperatures. The 3rd heating curves displayed a flattened shape and low-magnitude melting peaks where the melting process occurred over a broad temperature range.

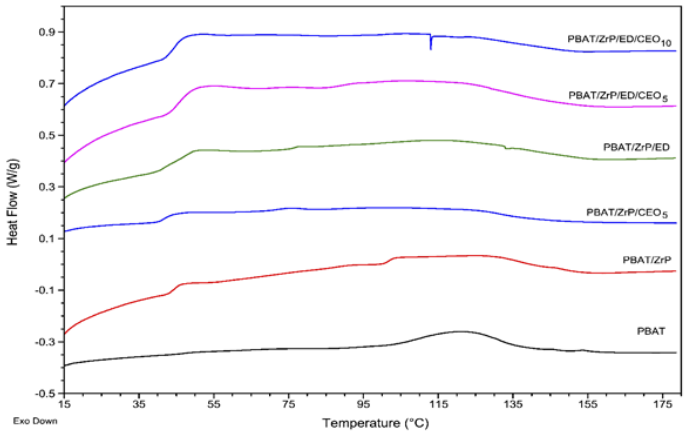

Figure 6a: DSC curves: 1st heating.

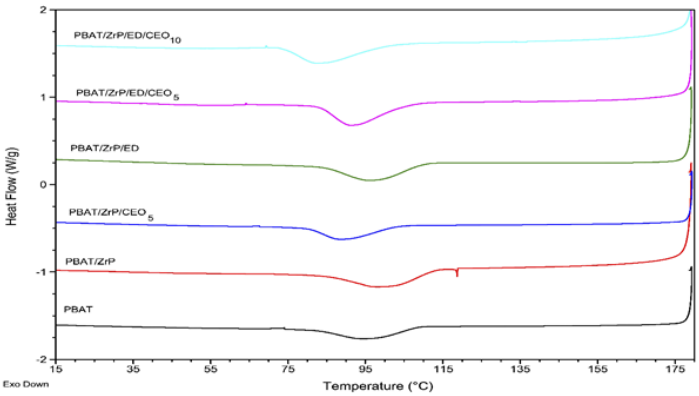

Figure 6b: DSC curves: 2nd cooling.

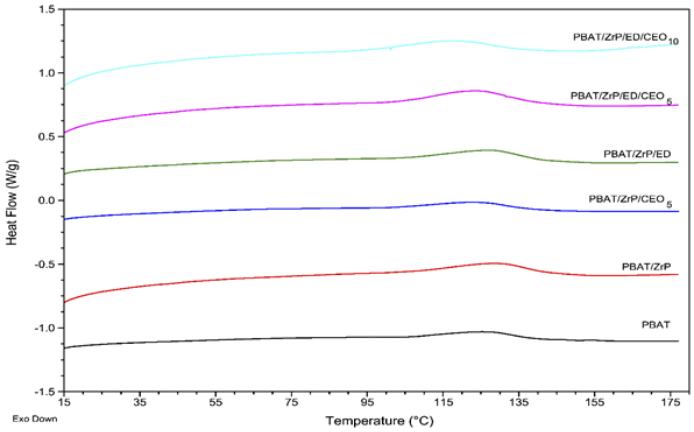

Figure 6c: DSC curves: 3rd heating.

Table 5 compiles the calorimetric data. As shown, the addition of phosphates shifted T_c to a higher temperature, while the incorporation of CEO caused the opposite behavior. T_m showed the same trend. For all composites, the degree of crystallinity (X_c) showed an increase of around 9-70%. Nanocomposites were developed by combining PBAT, 1-hexadecyl-3-methylimidazolium chloride ionic liquid (IL), and sodium montmorillonite nanoclay (MMT). Concerning calometric properties, both MMT and IL fomented an increase in PBAT crystallization and melting temperatures [44]. Luna et al. prepared films of PBAT embedded with thyme essential oil (1-20 wt.%) and observed that T_c tended to decrease, while T_m and X_c remained stable [45]. For both crystallization and melting, ΔT increased. In terms of crystallization, the ΔT balance indicated that phosphate and CEO shifted T_c to higher and lower temperatures, respectively. For melting, the variation of ΔT suggested that phosphate and CEO expanded the PBAT crystal formation interval. Although CEO acted as a retardant for PBAT crystallization, its effect on phosphate delamination is believed to have promoted heterogeneous crystallization of PBAT on the phosphate lamellae.

Wettability Evaluation

Figure 7 presents the sessile drop images and contact angle measurements. Except for PBAT/ZrP/ED/CEO_5, the composite images displayed droplets tending toward a spherical shape, indicating greater water repellence. In general, the incorporation of phosphates and CEO led to an increase in hydrophobicity. The addition of ZrP and ZrP/ED resulted in hydrophobicity increases of 19 and 23%, respectively. When CEO was added, PBAT/ZrP/CEO_5 and PBAT/ZrP/ED/CEO_{10} exhibited an increase of 51 and 27% in hydrophobicity, respectively, whereas PBAT/ZrP/ED/CEO_5 showed a value similar to PBAT. As reported by Rocha and collaborators, the opposite effect was found by incorporating zinc oxide and molybdenum trioxide into the PBAT matrix. The authors revealed that both oxides enhanced PBAT hydrophilicity, which could be considered an undesirable outcome for food packaging films [46]. Additionally, gum rosin (GR), a natural resin derived from pine trees, has been used to enhance hydrophobicity in PBAT films. Films containing this eco-resin were prepared by incorporating 5-15 wt.% to PBAT. The water wettability measurements indicated a hydrophobicity increase of 16-24%, attributed to the hydrophobic constituents of GR [47]. In conclusion, the increase of hydrophobicity is a crucial requirement for active films designed to prevent microorganism proliferation.

Table 5: DSC data.

Sample	T_c (°C)	Crystallization temperature interval (°C)	T_m(°C)	Melting temperature interval (°C)	ΔH_m (J/g)	X_c (%)
PBAT	94	79-109 (ΔT=30)*	126	108-138(ΔT=30)*	7.7	6.8
PBAT/ZrP	101	81-116(ΔT=35)	129	103-150(ΔT=47)	13.3	11.9
PBAT/ZrP/ED	97	80-115(ΔT=35)	128	101-145(ΔT=44)	12.5	11.2
PBAT/ZrP/CEO_5	89	73-111(ΔT=38)	124	102-144(ΔT=42)	8.5	7.4
PBAT/ZrP/ED/CEO_5	92	75-115(ΔT=40)	124	95-146(ΔT=51)	14.1	12.4
PBAT/ZrP/ED/CE_{O1}0	85	68-109(ΔT=41)	117	94-141(ΔT=47)	13.8	12.1

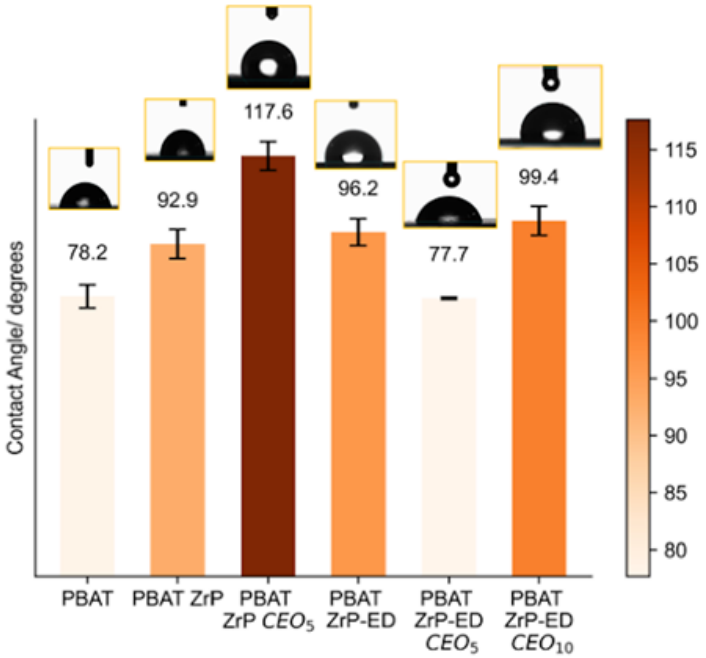

Figure 7: Sessile drop image and contact angle measurement.

Thermomechanical Analysis

Table 6 presents the glass transition temperature (T_g) and linear coefficient of thermal expansion (LCTE). The addition of both phosphates and CEO decreased the T_g. The LCTE behavior varied before and after T_g. Below T_g, the incorporation of phosphates and CEO resulted in a higher LCTE compared to PBAT alone across all composites. After T_g, the incorporation of ZrP increased LCTE, while ZrP/ED caused a decrease. No clear trend was observed regarding the influence of CEO. The results showed phosphate incorporation enhanced thermal conduction, while CEO addition generally reduced it.

Table 6: Samples' Tg and LCTE.

Sample	T_g (°C)	α before T_g (µm/m.°C)	α after T_g (µm/m.°C)
PBAT	-33	12.7	204.6
PBAT/ZrP	-37	70.8	235.3
PBAT/ZrP/CEO$_5$	-40	45.4	175.4
PBAT/ZrP/ED	-38	13.9	165.2
PBAT/ZrP/ED/CEO$_5$	-40	34.1	210.3
PBAT/ZrP/ED/CEO$_{10}$	-44	64.9	191.0

TD-nuclear Magnetic Resonance

As pointed out by Rocha et al. [46], the TD-NMR study allows for the investigation of microstructural molecular mobility of polymer chains. Figure 8 displays the distribution of time-domain relaxation curves and proton spin-lattice relaxation data. PBAT presented a single broad relaxation domain (T_1 = 56 ms). In contrast, PBAT/ZrP showed two distinct, narrower relaxation domains in the ranges of (1-2x10^4 and 4-8x10^4 ms), revealing T_1 values of 10 and 60 ms, respectively. The incorporation of CEO into PBAT/ZrP resulted in a relaxation curve similar to that of PBAT. The addition of ZrP/ED into PBAT did not alter its relaxation curve, but when CEO was mixed, two narrower relaxation domains emerged. The first appeared between 5-6x10^3, while the second ranged from 3-9x10^4, with T_1 values around 6 and 60 ms, respectively. The results indicated that the action of CEO on PBAT molecular mobility depended on the type of phosphate used. The results align with those obtained in the FTIR and WAXD analyses.

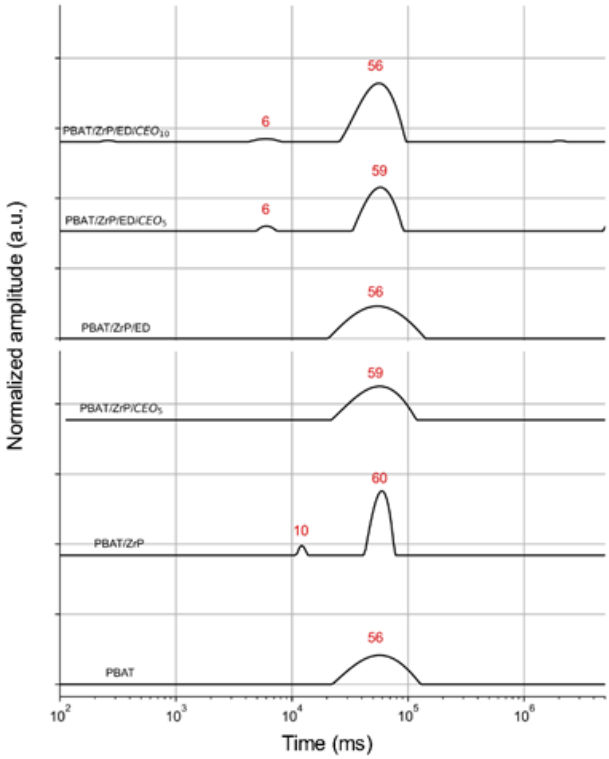

Figure 8: NMR time-domain relaxation curves and proton spin-lattice relaxation data.

Storage and loss moduli

Figure 9 exhibits the storage (E') and loss (E'') moduli curves in the temperature range of 30-95 °C. The incorporation of phosphates and CEO into PBAT resulted in a decrease in E' values, following the order: PBAT > PBAT/ZrP/ED ≈ PBAT/ZrP/ED/CEO$_5$ > PBAT/ZrP > PBAT/ZrP/ED/CEO$_{10}$. Similarly, E'' also decreased with the addition of both phosphates and CEO, with the gradation: PBAT > PBAT/ZrP ≈ PBAT/ZrP/ED ≈ PBAT/ZrP/ED/CEO$_5$ > PBAT/ZrP/ED/CEO$_{10}$. The effects of amine-expanding ZrP with different amine proportions and screw speeds were studied in polypropylene-based composites. At 60 rpm, all samples exhibited reductions in both E' and E'', attributed to ZrP particle dispersion and the interaction between polymer and phosphate [48]. Tavares et al. pointed out the increase of E' in PBAT composites embedded with kraft lignin, due to the formation of hydrogen bonding between PBAT and hydroxyl group of lignin matter [49]. Kilic et al. studied the composite of PLA/PBAT blend filled with epoxidized polyhedral oligomeric silsesquioxanes (Epoxy-POSS) and registered decreases in both storage and loss moduli, which were associated with poor interfacial adhesion and weak polymer-filler interactions [50]. To evaluate the effect of phosphates and

CEO on the viscoelastic properties of the composites, Table 7 presents the E”/E’ ratio at 40 °C. For all samples, the low values suggest that the components had minimal influence and that the elastic behavior predominated across the entire temperature range. Additionally, none of the components contributed to PBAT chain degradation.

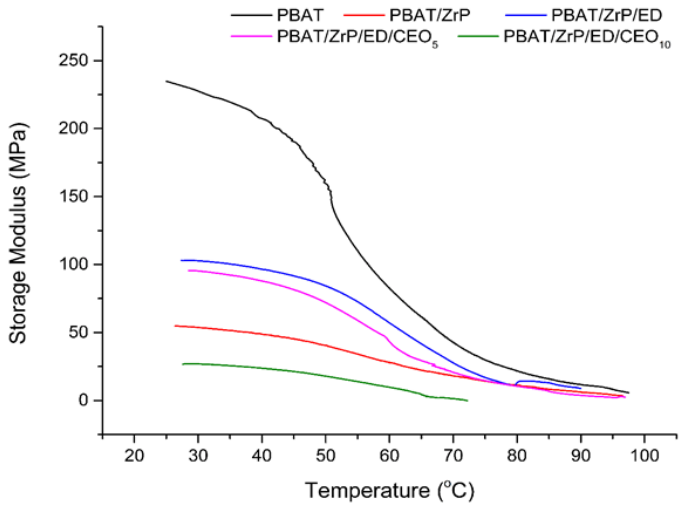

Figure 9a: Storage moduli.

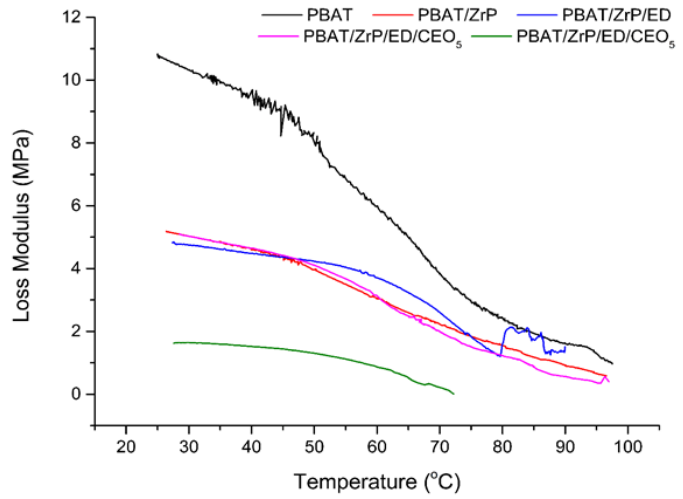

Figure 9b: loss moduli.

Table 7: Evaluation of E”/E’ at 40°C.

Sample	E”/E’
PBAT	0.047
PBAT/ZrP	0.094
PBAT/ZrP/ED	0.046
PBAT/ZrP/ED/CEO$_5$	0.053
PBAT/ZrP/ED/CEO$_{10}$	0.064

Antimicrobial Evaluation

Over the years, the medicinal and antimicrobial potential of cinnamon essential oil (*Cinnamomum verum*) has been attributed to the properties of its secondary metabolites, including cinnamaldehyde, eugenol, cinnamyl acetate, methyl cinnamate, (E)-caryophyllene, and linalool [51]. These components exhibit various mechanisms of action on cellular structures due to their lipophilic nature and low molecular weight. These mechanisms include cytoplasmic content leakage through cell membrane damage, reduction in ATP production, alteration of the pH gradient, loss of mitochondrial potential, and induction of cell death via apoptosis and/or necrosis. The resulting oxidative stress can damage biomolecules such as lipids, proteins, and nucleic acids, ultimately compromising cell viability [52]. CEO has been extensively studied for its antimicrobial properties, demonstrating activity against a variety of fungi and both Gram-positive (GPB) and Gram-negative bacteria (GNB) [53-57]. Additionally, it has been investigated for applications as an anticarcinogenic agent [58], in the production of antimicrobial nanofiber air filters,[59] for pest control in stored products [60], and more. In this study, only PBAT/ZrP/ED/CEO$_{10}$ exhibited bactericidal action, as presented in Table 8. The antibacterial action of the chemical components is commonly attributed to their ability to permeate the bacterial cell wall. As reported in some studies, the structural complexity of the GNB cell wall compared to GPB explains its higher resistance to hydrophobic antimicrobial compounds, including CEO [61-63]. In our study, no significant differences were observed between the bacterial groups tested. Hashim et al. explored the encapsulation of CEO within a biopolymer matrix. The incorporation of natural antimicrobial agents, such as cinnamon essential oil into polymeric matrices, has been explored in various applications, including biodegradable active food packaging [64]. Inhibition zones measuring 40.5 and 41.4 mm were achieved against *S. aureus* and *E. coli*, respectively [65]. Furthermore, spherical PBAT capsules containing CEO exhibited inhibition zones of 51.9 ± 0.5 mm against *S. Choleraesuis* and 55.3 ± 0.8 mm against *S. aureus*, as reported by Barbosa and collaborators [66]. Cyclodextrin sponges encapsulated with CEO have been tested as antimicrobial agents, exhibiting inhibition zones of approximately 49 mm against *L. monocytogenes* and *E. coli* [67].

Table 8: Antimicrobial activity of PBAT/ZrP/ED/CEO10 against bacteria and yeast

Microorganisms (ATCC[a] number)	Zone of inhibition (mm)
Gram-negative bacteria	
Escherichia coli 11229	14
Salmonella Enteritidis 13076	14
Pseudomonas aeruginosa 15442	12
Gram-positive bacteria	
Staphylococcus aureus 29213	14
Bacillus cereus 14579	14
Listeria monocytogenes 19117	12
Yeast	
Candida albicans 10231	32

[a] American Type Culture Collection

Further studies are needed to determine whether significant differences exist in the effects of these compounds against GPB and GNB, as well as the conditions that influence their antimicrobial activity. Additionally, PBAT/ZrP/ED/CEO$_{10}$ demonstrated more

pronounced antifungal activity compared to its antibacterial effect. This effect has also been reported by other authors against various *Candida* species [68], mycotoxin-producing fungi [69-70], and phytopathogenic fungi [71]. When combined, the wettability and antimicrobial results suggest that PBAT/ZrP/ED/CEO10 holds potential as an active and multifunctional packaging material.

Conclusions

Thinking about the non-proliferation of microplastics, alongside the goals prescribed in the UN 2030 Agenda, this work aimed to develop a composite based on a sustainable polymer filled with zirconium phosphate and CEO. Both materials influenced the molecular mobility of PBAT. Additionally, CEO interfered with the crystalline arrangement of the phosphate, which led to variations in PBAT wettability, degree of crystallinity, storage and loss moduli, and antimicrobial activity. Thus, an eco-friendly PBAT-based composite was developed, combining lower hydrophilicity and significant antimicrobial properties. This represents a promising approach for the food packaging sector, providing a film with effective barrier properties against pathogens and food-damaging microorganisms, thereby extending shelf-life.

Acknowledgments

The authors thank the Fundação Carlos Chagas Filho de Amparo à Pesquisa do Estado do Rio de Janeiro (FAPERJ) – Processo SEI E-26/200.814/202, the Conselho Nacional de Desenvolvimento Científico e Tecnológico (CNPq), the Fundação Coordenação de Aperfeiçoamento de Pessoal de Nível Superior (CAPES), and the Universidade Federal do Rio de Janeiro (UFRJ) for supporting this research.

References

1. The Sustainable Development Agenda - United Nations Sustainable Development.
2. Zhan X, Shang X, Zhou T, et al. Preparation and Properties of Triphenyl Octylphosphonium Bromide-modified Vermiculite and Its PBAT Composite Films. Polym Compos. 2024; 45: 12809-12818.
3. Guo Q, He Y, Wu J, et al. Sodium-Alginate-Doped Lignin Nanoparticles for PBAT Composite Films to Dually Enhance Tensile Strength and Elongation Performance with Functionality. Polymers (Basel). 2024; 16: 2312.
4. Wondu E, Lee G, Kim J, et al. Polybutylene Adipate Terephthalate (PBAT) Composites for Thermally Conductive, Fire Retardant, High Dielectric Applications Using BaTiO3 and Mwcnts as Fillers. Polym Test. 2024; 135: 108447.
5. Zhou SJ, Zhang D, Xiong SJ, et al. A High-Performance and Cost-Effective PBAT/Montmorillonite/Lignin Ternary Composite Film for Sustainable Production. ACS Sustain Chem Eng. 2024; 12: 14704-14715.
6. Techawinyutham L, Techawinyutham W, Rangappa SM, et al. Lignocellulose Based Biofiller Reinforced Biopolymer Composites from Fruit Peel Wastes as Natural Pigment. Int J Biol Macromol. 2024; 257: 128767.
7. Mei L, Lixian Z, Jialin Y, et al. Polylactic Acid/Poly(Butylene Adipate-Co-Terephthalate)/Diatomite Composites with Antimicrobial Properties for Green Packing. Polym Bull. 2023; 81: 1729-1742.
8. Kowalska J, Tyburski J, Matysiak K, et al. Cinnamon as a Useful Preventive Substance for the Care of Human and Plant Health. Molecules. 2021; 26: 5299.
9. Błaszczyk N, Rosiak A, Kałużna-Czaplińska J, et al. The Potential Role of Cinnamon in Human Health. Forests. 2021; 12: 648.
10. Kossyvaki D, Suarato G, Summa M. et al. Keratin–Cinnamon Essential Oil Biocomposite Fibrous Patches for Skin Burn Care. Mater Adv. 2020; 1: 1805-1816.
11. Han X, Parker TL. Antiinflammatory Activity of Cinnamon (Cinnamomum Zeylanicum) Bark Essential Oil in a Human Skin Disease Model. Phytother Res. 2017; 31: 1034-1038.
12. Moustafa H, Nasr HE, Youssef AM, et al. Development of Antibacterial Carboxymethyl Cellulose/Quaternized Starch Bionanocomposites Based on Cinnamon Essential Oil Nanoemulsion for Wound Healing Applications. Biomass Convers Biorefin. 2022;14: 27477-27489.
13. Hussein MA, Gunduz O, Sahin A, et al. Dual Spinneret Electrospun Polyurethane/PVA-Gelatin Nanofibrous Scaffolds Containing Cinnamon Essential Oil and Nanoceria for Chronic Diabetic Wound Healing: Preparation, Physicochemical Characterization and in-Vitro Evaluation. Molecules. 2022; 27: 2146.
14. Zhu Z, Baker J, Liu C, et al. High Performance Epoxy Nanocomposites Based on Dual Epoxide Modified α-Zirconium Phosphate Nanoplatelets. Polymer. 2021; 212: 123154.
15. Silva BN, Tavares SR, Leitão AA, et al. Exfoliation of Zirconium Aminophosphonates: Investigation into Their Electronic Structures by Ab Initio Calculations. New J Chem. 2020; 44: 10111-10118.
16. Xiao H, Liu S. Zirconium Phosphate (ZRP)-Based Functional Materials: Synthesis, Properties and Applications. Mater Des. 2018; 155: 19-35.
17. Zhang J, Fu X, Cai W, et al. Surface Functionalization of Zirconium Phosphate via Sol-Gel Chemistry for Optimizing Fire Safety and Mechanical Property of poxy/Intumescent Flame Retardant Composites. Thermochim Acta. 2023; 729: 179609.
18. Xu F, Zhang H, Wu J, et al. Synergistic Catalytic Flame Retardant Effect of Zirconium Phosphate on the Poplar Plywood. Constr Build Mater. 2021; 290: 123208.
19. Zhang H, Li K, Wang M, et al. The Preparation of a Composite Flame Retardant of Layered Double Hydroxides and α-Zirconium Phosphate and Its Modification for Epoxy Resin. Mater. Today Commun. 2021; 28: 102711.
20. Zheng P, Zhao H, Li J. et al. Flame Retardant Based on Metal Catalyzed Instantaneous Crosslinking to Form Carbon for Improving the Safety Performance of Aircraft Epoxy Resin. Saf Sci. 2024; 178: 106627.

21. Wang C, Huo S, Ye G, et al. Phenylboronic Acid-Decorated ZRP Nano sheets for Enhancing Fire Resistance, Smoke Suppression, and Water/Acid/Alkali Tolerance of Intumescent Coatings. Colloids Surf. A: Physicochem. Eng Asp. 2022; 655: 130292.
22. Wang C, Huo S, Ye G, et al. Phosphaphenanthrene Modified Zirconium Phosphate Nano sheets for Improving Fire Resistance, Smoke Suppression and Water Tolerance of Intumescent Coatings. J Coat Technol Res. 2023; 20: 1353-1367.
23. Han S, Yang F, Li Q, et al. Synergetic Effect of α-ZRP Nanosheets and Nitrogen-Based Flame Retardants on Thermoplastic Polyurethane. ACS Appl. mater Interfaces. 2023; 15: 17054-17069.
24. Guan J, Wei Z, Yan L, et al. Construction of Organophosphate-Functionalized A-zirconium Phosphate towards Fire-Resistant, Weather-Resistant and Antibacterial Reinforcement of Transparent Fireproof Coatings Applied on Wood Substrates. Prog Org Coat. 2024; 190: 108397.
25. Wang M, Xiao G, Chen C, et al. Synergistic Enhancement of Flame Retardancy of Epoxy Resin by Layered Zirconium Phenylphosphate Modified Layered Double Hydroxides. Prog Org Coat. 2023; 177: 107437.
26. Han S, Li S, Liu D, et al. Enhancing Flame Retardancy, Anti-impact, and Corrosive Resistance of Tpu Nanocomposites Using Surface Decoration of A-zrp. Polym Compos. 2024; 45: 9209-9223.
27. Albitres G, Garcia E, Soares C, et al. Post-Consumer High DensityPolyethylene/Zirconium Phosphate and Aluminum Hydroxide Composites: Assessment of Physico-Mechanical and Flame Retardancy Properties. J Compos Mater. 2024; 58: 489-503.
28. Kojima S, Lee S, Nagata F, et al. Protein Immobilisation onto Zirconium Phosphate with the Enhancement of the Adsorption Amount and Catalytic Activity. Mater Today Commun. 2020; 25: 101310.
29. Zhu Z, Baker J, Liu C, et al. High Performance Epoxy Nanocomposites Based on Dual Epoxide Modified α-Zirconium Phosphate Nanoplatelets. Polymer. 2021; 212: 123154.
30. Martins BM, Garcia EE, Albitres GA, et al. Dental Post Based on Epoxy Resin/Zirconium Phosphate Composite Aiming Prosthetic Dentistry. Mater Sci Appl. 2024; 15: 504-527.
31. Mendes LC, Silva DF, Araujo LJ, et al. Zirconium Phosphate Organically Intercalated/Exfoliated with Long Chain Amine. J Therm Anal Calorim. 2014; 118: 1461-1469.
32. Xiao H, Lu W, Yeh J, et al. Crystallization Behavior of Fully Biodegradable Poly(Lactic Acid)/Poly(Butylene Adipate-Co-terephthalate) Blends. J Appl Polym Sci. 2009; 112: 3754-3763.
33. International Organization for Standardization, Plastics — Thermomechanical analysis (TMA) Part 2: Determination of coefficient of linear thermal expansion and glass transition temperature. ISO Standard No. 11359-2:2021.
34. Sim JY, Raj CJ, Yu KH, et al. Poly (Butylene Adipate-co-terephthalate) (PBAT)/Antimony-doped Tin Oxide Polymer Composite for near Infrared Absorption Coating Applications. Bull. Korean Chem Soc. 2019; 40: 674-679.
35. Li Y, Kong D, Wu H, et al. Analysis and Evaluation of Essential Oil Components of Cinnamon Barks Using GC–MS and FTIR Spectroscopy. Ind Crops Prod. 2013; 41: 269-278.
36. Li T, Zhu Z, Zhou S, et al. Preparation of P-CdS Functionalized α-ZRP Flake Fillers and Enhancing Anti-Corrosion Properties of Epoxy Coating. Prog Org Coat. 2024; 196: 108733.
37. Yan L, Yan S, He Y, et al. Effects of Propylamine and Ethylenediamine Intercalation of α-ZRP on the Corrosion Resistance and Tribological Properties of Electroless Ni-B Coatings. Surf Coat Tech. 2023; 471: 129883.
38. Yamaguchi M, Miyaoka H, Kojima Y, et al. Thermodynamic and Spectroscopic Analyses of Zirconium Phosphate-Absorbed Ammonia. J Phys Chem C. 2021; 125: 3758-3763.
39. Fukushima K, Wu MH, Bocchini S, et al. PBAT Based Nanocomposites for Medical and Industrial Applications. Mater Sci Eng C. 2012; 32: 1331-1351.
40. J Frache A, Flame Retardancy Properties of α-Zirconium Phosphate Based Composites. Polym Degrad Stab. 2010; 95: 1928-1933.
41. Venkatesan R, Alagumalai K, Jebapriya M, et al. Enhancing Pbat Nanocomposite Films: The Impact of Agvo3 Nanorods on Mechanical, Hydrophobicity and Antibacterial Properties. Polym Compos. 2024; 45: 15340-15355.
42. Singh S, Pereira J, Guerreiro, et al. Safety Profile of ZnO Active Packaging PBAT Based Biomaterial for Food Packaging. First Tier Evaluation. Food Control. 2024; 161: 110389.
43. Han M, Qin Z, Wang J. et al. Preparation of Polybutylene Adipate Terephthalate/Tannic Acid-ZnO Nanocomposite Films with Excellent UV Shielding, Antioxidant and Antibacterial Activities. LWT. 2025; 215: 117239.
44. Sui X, Wang Z, Yan S, et al. Performance Improvement of Poly (Butylene Adipate-Butylene Terephthalate) Based Nanocomposites Modified by the Cooperation of Nano Montmorillonite and Ionic Liquid. J Polym Res. 2024; 31.
45. Luna PB, Caetano VF, Andrade MF, et al. Effect of Thyme Essential Oil on the Properties of Poly (Butylene Adipate-Co-Terephthalate) (Pbat). Polímeros. 2024; 34.
46. da Rocha LV, da Silva PS, da Silva EM, et al. Biodegradable Packing Food Films Based on PBAT Containing ZnO and MoO_3. J Appl Polym Sci. 2024; 141.
47. Pavon C, Aldas M, Rosa-Ramírez H, et al. Improvement of PBAT Processability and Mechanical Performance by Blending with Pine Resin Derivatives for Injection Moulding Rigid Packaging with Enhanced Hydrophobicity. Polymers (Basel). 2020; 12: 2891.
48. Mariano D de, Freitas D de, Mendes LC, et al. Nano Lamellar Zirconium Phosphate and Screw Speed Changing Properties of Melt Extrusion Polypropylene Nanocomposites. J Compos Mater. 2021; 55: 2443-2458.

49. Tavares LB, Ito, NM, Salvadori MC, et al. PBAT/Kraft Lignin Blend in Flexible Laminated Food Packaging: Peeling Resistance and Thermal Degradability. Polym Test. 2018; 67: 169-176.
50. Kilic NT, Can BN, Kodal M, et al. Compatibilization of PLA/PBAT Blends by Using Epoxy-poss. J Appl Polym Sci. 2018; 136.
51. Singh N, Rao AS, Nandal A, et al. Phytochemical and Pharmacological Review of Cinnamomum Verum J. Presl-a Versatile Spice Used in Food and Nutrition. Food Chem. 2021; 338: 127773.
52. Sharifi-Rad J, Sureda A, Tenore G, et al. Biological Activities of Essential Oils: From Plant Chemoecology to Traditional Healing Systems. Molecules. 2017; 22: 70.
53. Padalia H, Rathod T, Moteriya P, et al. Antimicrobial Efficacy of CINNAMONUM Verum Essential Oil Alone and in Combination with Antibiotics and Other Essential Oils. Int J Curr Microbiol. Appl. Sci. 2017; 6: 3377-3395.
54. Patterson JE, McElmeel L, Wiederhold NP, et al. In Vitro Activity of Essential Oils against Gram-Positive and Gram-Negative Clinical Isolates, Including Carbapenem-Resistant Enterobacteriaceae. Open Forum Infect. Dis. 2019; 6.
55. Sayed MA, Ghazy, Nahla M, et al. Synergistic Potential of Essential Oil Combinations against Microsporum, Trichophyton, and Epidermophyton. Int Microbiol. 2024.
56. Clemente I, Aznar M, Nerín C, et al. Synergistic Properties of Mustard and Cinnamon Essential Oils for the Inactivation of Foodborne Moulds in Vitro and on Spanish Bread. Int J Food Microbiol. 2019; 298: 44-50.
57. Roy S, Rhim JW. Fabrication of Bioactive Binary Composite Film Based on Gelatin/Chitosan Incorporated with Cinnamon Essential Oil and Rutin. Colloids Surf B Biointerfaces. 2021; 204: 111830.
58. Srilatha K, Deshmukh S, Gandhi HA, et al. Comparison of Antimicrobial Efficacy of Cinnamon Bark Oil Incorporated and Probiotic Blend Incorporated Mucoadhesive Patch against Salivary Streptococcus Mutans in Caries Active 10-Year-Old Children: An in Vivo Study. Int J Clin Pediatr Dent. 2020; 13: 543-550.
59. Son BC, Park CH, Kim CS, et al. Fabrication of Antimicrobial Nanofiber Air Filter Using Activated Carbon and Cinnamon Essential Oil. J Nanosci Nanotechnol. 2020; 20: 4376-4380.
60. Mahdavi V, Rafiee-Dastjerdi H, Asadi A, et al. Management of the Phthorimaea Operculella (Zeller) Using PVA Nanofibers Loaded with Cinnamomum Zeylanicum Essential Oil. Am J Potato Res. 2017; 94: 647-657.
61. Patterson JE, McElmeel L, Wiederhold NP, et al. In Vitro Activity of Essential Oils against Gram-Positive and Gram-Negative Clinical Isolates, Including Carbapenem-Resistant Enterobacteriaceae. Open Forum Infect. Dis. 2019; 6.
62. Van de Vel E, Sampers I, Raes K, et al. A Review on Influencing Factors on the Minimum Inhibitory Concentration of Essential Oils. Crit Rev Food Sci Nutr. 2017; 59: 357-378.
63. Tavares TD, Antunes JC, Padrão J, et al. Activity of Specialized Biomolecules against Gram-Positive and Gram-Negative Bacteria. Antibiotics (Basel). 2020; 9: 314.
64. Díaz-Galindo EP, Nesic A, Bautista-Baños S, et al. Corn-Starch-Based Materials Incorporated with Cinnamon Oil Emulsion: Physico-Chemical Characterization and Biological Activity. Foods. 2020; 9: 475.
65. Hashim SBH, Tahir HE, Mahdi, et al. Fabrication of Biopolymer Stabilized Microcapsules for Enhancing Physicochemical Stability, Antioxidant and Antimicrobial Properties of Cinnamon Essential Oil. Int J Biol Macromol. 2024; 271: 132336.
66. Barbosa RF, Yudice ED, Mitra SK, et al. Characterization of Rosewood and Cinnamon Cassia Essential Oil Polymeric Capsules: Stability, Loading Efficiency, Release Rate and Antimicrobial Properties. Food Control. 2021; 121: 107605.
67. Simionato I, Domingues FC, Nerín C, et al. Encapsulation of Cinnamon Oil in Cyclodextrin Nanosponges and Their Potential Use for Antimicrobial Food Packaging. Food Chem Toxicol. 2019; 132: 110647.
68. Choonharuangdej S, Srithavaj T, Thummawanit S, et al. Fungicidal and Inhibitory Efficacy of Cinnamon and Lemongrass Essential Oils on Candida Albicans Biofilm Established on Acrylic Resin: An in Vitro Study. J Prosthet Dent. 2021; 125.
69. Minozzo M, de Souza MA, Bernardi, et al. Antifungal Activity and Aroma Persistence of Free and Encapsulated Cinnamomum Cassia Essential Oil in Maize. Int J Food Microbiol. 2023; 394: 110178.
70. Reis KL dos, Barbosa-Tessmann IP. Research Article Genetic Variability of Aspergillus Flavus Isolated from Commercial Peanut and Bulgur Wheat in Southern Brazil and Antifungal Activity of Essential Oils against Some of the Isolates. Genet Mol Res. 2021; 20.
71. Lee JE, Seo SM, Huh MJ, et al. Reactive Oxygen Species Mediated-Antifungal Activity of Cinnamon Bark (Cinnamomum Verum) and Lemongrass (Cymbopogon Citratus) Essential Oils and Their Constituents against Two Phytopathogenic Fungi. Pestic Biochem Physiol. 2020; 168: 104644.